BBA - Molecular Basis of Disease 1869 (2023) 166840

Contents lists available at ScienceDirect

BBA - Molecular Basis of Disease

journal homepage: www.elsevier.com/locate/bbadis

Fourier transform IR imaging of primary tumors predicts lymph node metastasis of bladder carcinoma

Monika Kujdowicz [a,b], David Perez-Guaita [c], Piotr Chlosta [d], Krzysztof Okon [a], Kamilla Malek [b,*]

[a] Department of Pathomorphology, Faculty of Medicine, Jagiellonian University Medical College, Grzegorzecka 16, 31-531 Krakow, Poland
[b] Department of Chemical Physics, Faculty of Chemistry, Jagiellonian University in Kraków, Gronostajowa 2, 30-387 Krakow, Poland
[c] Department of Analytical Chemistry, University of Valencia, 50 Dr Moliner Street, Research Building, 46100 Burjassot, Valencia, Spain
[d] Department of Urology, Faculty of Medicine, Jagiellonian University Medical College, Jakubowskiego 2, 30-688 Krakow, Poland

ARTICLE INFO

Keywords:
Bladder carcinoma
Lymph node metastasis
Fourier transform infrared spectroscopic imaging
Chemometric analysis
Prediction mode

ABSTRACT

The process of metastasis is complex and often impossible to be recognized in conventional clinical diagnosis. Lymph node metastasis (LNM) of bladder carcinoma (BC) is often associated with muscle-invasive tumors. To prevent and recognize LNM, the standard treatment includes radical cystectomy with lymph node dissection and histological examination. Here, we propose infrared (IR) microscopy as a tool for the prediction of LNM. For this purpose, IR images of bladder biopsies from patients with diagnosed non-metastatic early (E BC) and advanced (A BC), as well as metastatic advanced (M BC) bladder cancer were first collected. Furthermore, this dataset was complemented with images of the secondary tumors from the lymph nodes (M LN) of the M BC patients. Unsupervised clustering was used to extract tissue structures from IR images to create a data set comprising 382 IR spectra of non-metastatic bladder tumors and 241 metastatic ones. Based on that, we next established discrimination models using PLS-DA with repeated random sampling double cross-validation, and permutation test to perform the classification. The accuracy of BC metastasis prediction from IR bladder biopsies was 83 % and 78 % for early and advanced BC, respectively, herein demonstrating a proof-of-concept IR detection of BC metastasis. The analysis of spectral profiles additionally showed molecular composition similarity between metastatic bladder and lymph node tumors. We also determined spectral biomarkers of LNM that are associated with sugar metabolism, remodeling of extracellular matrix, and morphological features of cancer cells. Our approach can improve clinical decision-making in urological oncology.

1. Introduction

Bladder urothelial carcinoma (BC) ranks as the tenth malignancy in the world. Malignant behavior is generally defined as the presence of invasion, recurrences, and metastases. Although BC metastases are rare, they significantly impair patient outcomes and require radical cystectomy, chemo- and radiotherapy, in addition to standard surgery and BCG therapy (the application of attenuated Bacillus Calmette-Guérin bacteria) [1,2]. Chemotherapy includes the use of cisplatin and vinca alkaloids (vinflunine) often combined with immunotherapy with anti-PDL-1 inhibitors (pembrolizumab, avelumab) or nectin antibody (enfortumab) [3–5]. It is usually introduced into the treatment of advanced BC stages without a priori knowledge if metastasis is present. Several genetic and epigenetic factors have been also determined and investigated to recognize the mechanisms underlying BC invasion and metastasis as well as to predict response to therapy [6,7]. Approximately 70 % of BC metastases are synchronous and appear firstly in regional, and then in distant lymph nodes and next cancer cells migrate to bones, lungs, liver, and brain [8]. Metastases to lymph nodes are present in ca. 25 % of cases of muscle-invasive bladder carcinoma [3]. Only large metastases can be detected by radiological methods and differentiated from reactive changes of lymph nodules [8]. Therefore, patients with advanced BC stages require a priori lymphadenectomy, and then tissue samples are examined by histopathologists to detect metastasis.[3]

Abbreviations: BC, bladder urothelial carcinoma; A BC, advanced BC; E BC, early BC; M BC, BC which gave metastasis to lymph nodule; HG BC, high-grade BC; LG BC, low-grade BC; FTIR, Fourier Transform Infrared spectroscopy; PCA, principal component analysis; PLS-DA, partial least squares discriminant analysis; UHCA, unsupervised hierarchical cluster analysis; ROC, receiver operating characteristic; Ve, vector; vs, versus.

* Corresponding author.
E-mail address: kamilla.malek@uj.edu.pl (K. Malek).

https://doi.org/10.1016/j.bbadis.2023.166840
Received 5 April 2023; Received in revised form 30 June 2023; Accepted 4 August 2023
Available online 7 August 2023

Unfortunately, lymphadenectomy is accompanied by numerous side effects such as post-operative pain, wound infections, wound edge necrosis, suppuration and dehiscence of the wound edges, hematomas, lymph cysts, lymphorrhea, rare venous thrombosis as well as edema of the lower limbs [9]. This issue implies the need for the early recognition of BC metastasis and an understanding of molecular mechanisms to develop tools to support the clinical assessment.

The primary tumor can form a secondary tumor, and that ability of the primary tumor is called metastatic potential. Some cancers (e.g., breast cancer) can metastasize at their very early phases of progression or even many years after excision, while others (e.g., bladder carcinoma) have a high risk of metastasis mainly at an advanced stage. The metastasis process requires enzymatic breakage of the tissue stroma, angioinvasion, and the appropriate pre-metastatic niche in metastatic organs. The BC progression and metastasis are not simple to be predicted because of the heterogeneous features of this cancer as well as the organ and immune system [1,10]. For this reason, bladder carcinoma remains mostly an incurable disease at the advanced stage. In clinics, hematoxylin-eosin staining (HE) of excision from the bladder collected in cystoscopy is first assessed by pathologists but without indication of the tumor malignancy. Metastases are detected by using radiological techniques (CT, NMR, PET) or after the total bladder excision with lymphadenectomy. In the latter, the excised lymphoid tissue is again assessed by pathologists. So far, no method would predict the metastasis potential in early BC diagnosis.

Fourier-transformed infrared (FTIR) microscopy has emerged as a powerful tool in the clinical context as it simultaneously recognizes all biochemical components through signals generated by vibrations of the chemical groups. Several reports have demonstrated the capability of FTIR-based classification models to identify many types of metastases to the abdominal peritoneum (e.g., gastric, ovarian, and colon cancer), as well as to detect metastasis of papillary thyroid cancer to lymph nodes [11–13]. The great potential of FTIR spectroscopy has been also reported in studies on pulmonary metastasis of breast carcinoma in a murine model [14–17]. Here, FTIR microscopy has been successfully applied for the detection of micrometastases. In addition, spectral profiles have visualized and quantified structural modifications in the extracellular matrix (ECM) in lungs occurring due to the progression of metastasis.

Our recent works have evidenced that FTIR spectroscopy is useful for the support of the BC diagnosis from samples of urine sediment, cytology, and biopsy, including invasion and grade recognition [18–20]. We have continued our studies shown in this article to examine the capability of FTIR microscopy to recognize bladder carcinoma metastasis. We aimed to determine spectral markers found in IR spectra of the bladder specimens which could give an insight into metabolic pathways associated with BC metastasis. We tested the spectra in terms of a classification approach to predict cancer cell invasion to regional lymph nodes. For this purpose, we investigated bladder tumors from two groups of patients with diagnosed advanced BC stage and clinically proven metastasis status in the lymph nodes, i.e. A BC – advanced BC without metastasis and M BC – advanced BC with metastasis. The control group included bladder tumors from the non-metastatic early stage (E BC). In addition, we compared M BC spectral profiles with the secondary tumors in the lymph nodes (M LN) to assess to what extent the overall biochemical composition of the primary tumor is preserved upon migration of cancer cells. The potential clinical implementation of our results is the prediction of metastasis based on small bladder tissue samples to help clinicians (oncologists and urologists) in planning the appropriate treatment.

2. Materials and methods

2.1. Ethical consent

The study was reviewed and accepted by the First Local Ethics Committee of the Jagiellonian University Medical College in Krakow (No. 1072.6120.100.2018). Patient consent to medical procedure necessary for diagnosis or treatment of bladder tumor was taken before biopsy or cystectomy. The additional consent to use anonymized paraffin tissue fragments was not necessary, as we used only the remainder of the sample after standard diagnostics.

Table 1
Clinical characteristics of 40 patients with clinical classification.

	E BC	A BC	M BC and M LN
No. patients (female:male)	13 (7:6)	18 (2:16)	9 (1:8)
Average age (SD)	67.5 (11.4)	70.1 (6.9)	65.6 (8.6)
LG/HG BC	12/1	6/12	0/9
Papillary growth	8	5	2

E BC and A BC – non-metastatic early and advanced BC, respectively, M BC – advanced and metastatic BC with metastasis in lymph nodes (M LN), SD – standard deviation; LG/HG BC – low and high-grade bladder carcinoma, respectively.

2.2. Sample collection and clinical classification

The clinical characteristics of forty patients are listed in Table 1. Bladder excisions and lymph nodes were collected during surgical procedures performed in the Department of Urology of the Jagiellonian University Medical College (UJ CM) according to guidelines of the European Association of Urology [2]. The inclusion criterion was adult, and the exclusion criteria were pregnancy, history of radiotherapy in the pelvic region, and bladder cancer other than the urothelial type. Tissue fragments were fixed with 4 % buffered formalin, and embedded in paraffin, and adjacent cross sections were placed on CaF_2 windows for IR imaging and glass slides for hematoxylin/eosin (HE) staining. Sections were prepared at a thickness of 7 μm. Photographic documentation was collected using an Olympus BX53 light microscope equipped with an Olympus DP27 digital camera (Department of Pathomorphology, UJ CM). A histopathological assessment was performed according to the WHO 2017 guidelines [21]. The patients were assigned to three groups, i.e., early (E BC) and advanced (A BC) bladder carcinoma without lymph node metastasis, and BC with metastases (M BC), see Table 1. The high-grade patients (HG BC) had undergone lymphadenectomy (herein from A BC and M BC groups). In the case of any metastasis to lymph nodes (27 nodes from M BC patients only), secondary tumors (M LN) were also investigated. The number of metastases varied from 1 to 6 per patient.

2.3. FTIR spectroscopic imaging

The deparaffinized tissue cross-sections deposited on the CaF_2 windows were imaged with an FTIR Agilent 670-IR spectrometer coupled with a 620-IR microscope (Agilent Technologies, Santa Clara, CA, USA). The spectrometer was equipped with a 128 × 128 grid focal plane array (FPA) detector and Cassegrain objective 15× (NA: 0.62). The transmission mode with a pixel size of 5.5 μm × 5.5 μm was used. FTIR spectra were recorded by co-adding 32 scans in the range of 3700–900 cm^{-1} with a spectral resolution of 4 cm^{-1}. The tumor size is related to the stage and the surgical resection method (transurethral resection or cystectomy). In most cases of E BC and A BC, an area of one tissue fragment was ca. 4900 μm × 3500 μm. In the cases of M BC collected during cystectomy, IR images from different sites of a 2800 μm × 2800 μm area were acquired and they included the border of the tumor with nonneoplastic urothelium, borders of invasion, the central area of the tumor and an area where HE morphology was markedly different (in total 27 IR images). An area of the metastatic tumor in the lymph node (M LN) was ca. 2800 μm × 2800 μm. A schematic of our approach is presented in Fig. 1.

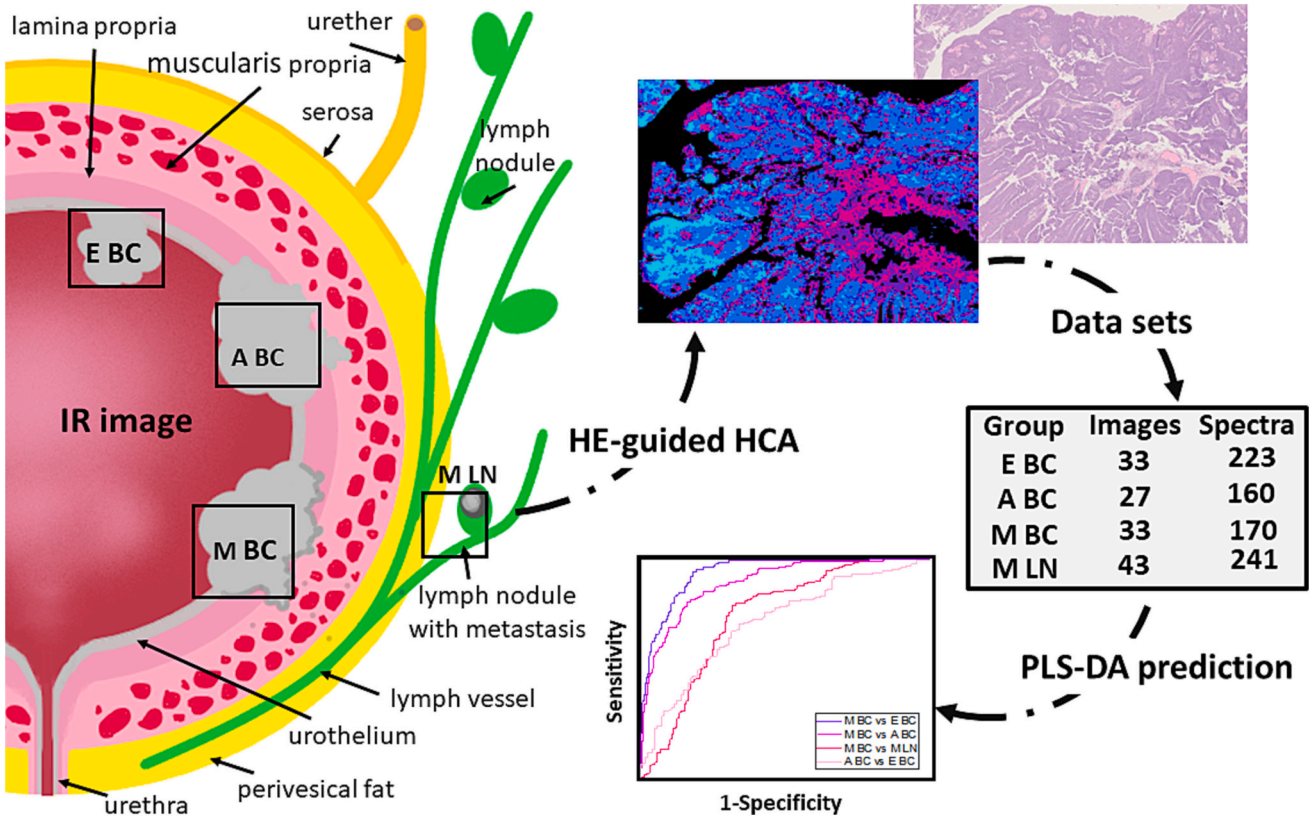

Fig. 1. A schematic of the workflow employed in this work.

2.4. Data acquisition and pre-treatment

Pre-processing and chemometric analysis of the collected FTIR images was performed using the following methods: CytoSpec (ver. 2.00.01) [22], MATLAB (R2021a, MathWorks, Natick, MA, USA), Unscrambler X (v. 10.5, Camo, Montclair, NJ, USA), Opus 7.0 (Bruker Optics, Version 7.2.139.1294), and Origin 9.1 (ver. 2020b, OriginLab, OriginLab Corporation, Northampton, MA, USA) software. Partial least squares discriminant analysis (PLS-DA) was performed using in-house written scripts based on the function from the PLS_Toolbox library from Eigenvector Research Inc. (Washington, MA, USA). Scripts and datasets are available at the Zenodo repository.

Firstly, the removal of water vapor lines, quality test (based on signal-to-noise ratio in the regions of 1700–1600 and 1800–1900 cm^{-1}, respectively), PCA-based denoising (10 PCs), calculation of the second derivative (Savitzky-Golay; 13 points) and vector normalization (spectral region of 1780–1000 cm^{-1}) was performed. Unsupervised hierarchical cluster analysis (UHCA; CytoSpec, MATLAB) was executed in the 1780–1000 cm^{-1} region. Spectral distances were calculated as D-values. Classes were computed according to a Ward algorithm. The number of UHCA classes was adjusted according to the tissue morphology in the HE images. The extracted mean FTIR spectra were used for building models and their verification. For this purpose, we collected spectra only from a tumor area defined as a mixture of cancer cells with their matrix, excluding fibrous or muscle tissue fragments larger than two pixels (ca. 11 μm). Usually, more than one class was assigned to the tumor, but our approach was also designed to reveal intratumoral spectral heterogeneity. The total number of spectra extracted from UHCA maps was 223 (E BC), 160 (A BC), 170 (M LN), and 241 (M BC). Integral intensities of selected IR bands in the second derivative spectra were calculated using the Opus software. Then, their box charts were constructed. An analysis of variance was performed using the ANOVA statistical model, while significance (*p*-values) was determined by Tukey's test (OriginLab).

2.5. Model building and testing

Firstly, we aimed to obtain an initial assessment of the classification performance and investigate the bands responsible for the discrimination in regression vectors. To that end, PLS-DA models were carried out using leave-on-patient-out cross-validation (LOPO-CV) for the selection of the best preprocessing and the optimal number of latent variables. For all the models, the 950–1800 cm^{-1} region was considered. For each classification, models combining derivatives (first and second) and normalizations (Standard Normal Variate [SNV] and Extended Multiplicative Scattering Correction [EMSC]) were created. Models were built using LVs values from 1 to 10, and the model with the lowest LOPO-CV was chosen. It must be noted that, if a large number of LVs provided just a small improvement of the error, the model selected was the one with a low number of LVs. The statistical significance of the model was evaluated using a permutation test, and the regression vector of the model [23]. Secondly, to study the generalization performance of the model, repeated random sampling double cross-validation was employed. Second derivative FTIR spectra followed by SNV and mean centering were used as preprocessing steps. Several spectra were measured in each sample. The data was split at the patient level during the entire process to avoid the replicate sample trap. In the outer loop, patients were randomly divided between the calibration (66 %) and test (33 %) sets. In the inner loop, the calibration set of patients was used to create a PLS-DA model, using LOPO-CV to choose the optimal number of LVs. The model was then validated using the test set of patients not included in the calibration. This process was repeated 100 times with different calibration and test samples, recording figures of merit such as sensitivity, specificity, accuracy, and the area under the Receiver Operating Characteristic (AUROC). The classifications considered were M BC versus E BC, A BC and M, LN, as well as A BC versus E BC.

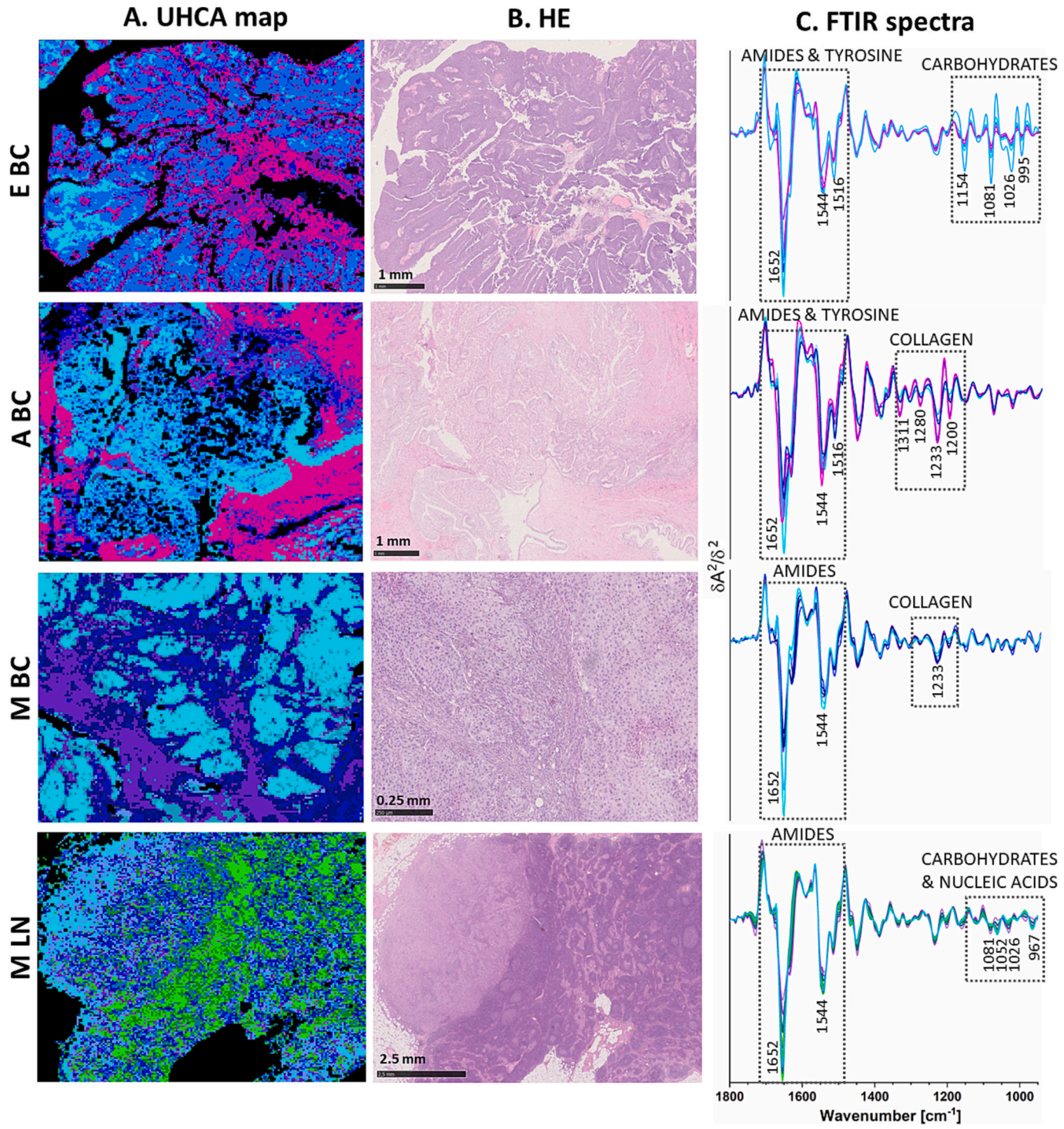

Fig. 2. Comparison of the false-color UHCA cluster maps (column A) and the corresponding histological HE stains (column B) of tumors with the surrounding tissue in the bladder (E, A, and M BC) and lymph node (M LN). The corresponding second derivative FTIR spectra (column C) extracted from UHCA maps in (B); the colors of the spectra correspond to the colors of the UHCA classes. Marked spectral regions in (C) highlight intratumor biochemical diversity revealed by UHCA classes. Color code: cyan, blue, purple – tumor IR classes, pink – bladder tissue without cancer cells, and green – cellular structures of the lymph node without cancer cells (predominantly lymphocytes as well as macrophages and histiocytes).

3. Results and discussion

3.1. IR-based morphology of tumors

Each IR image was first processed by using Unsupervised Hierarchical Cluster Analysis (UHCA) to reduce the hyperspectral database and combine FTIR spectra with a similar profile as classes. As a result, sets of mean spectra were calculated for each experimental group and further used in their description and classification models. The number of classes applied in cluster analysis was guided by the histopathological examination of HE stains. In that way, we distinguished the primary and secondary tumors in the bladder walls and lymph nodes, respectively, from the surrounding tissue matrix (Fig. 2). In each examined tissue cross-section, we obtained a clear demarcation of the tumors that shows

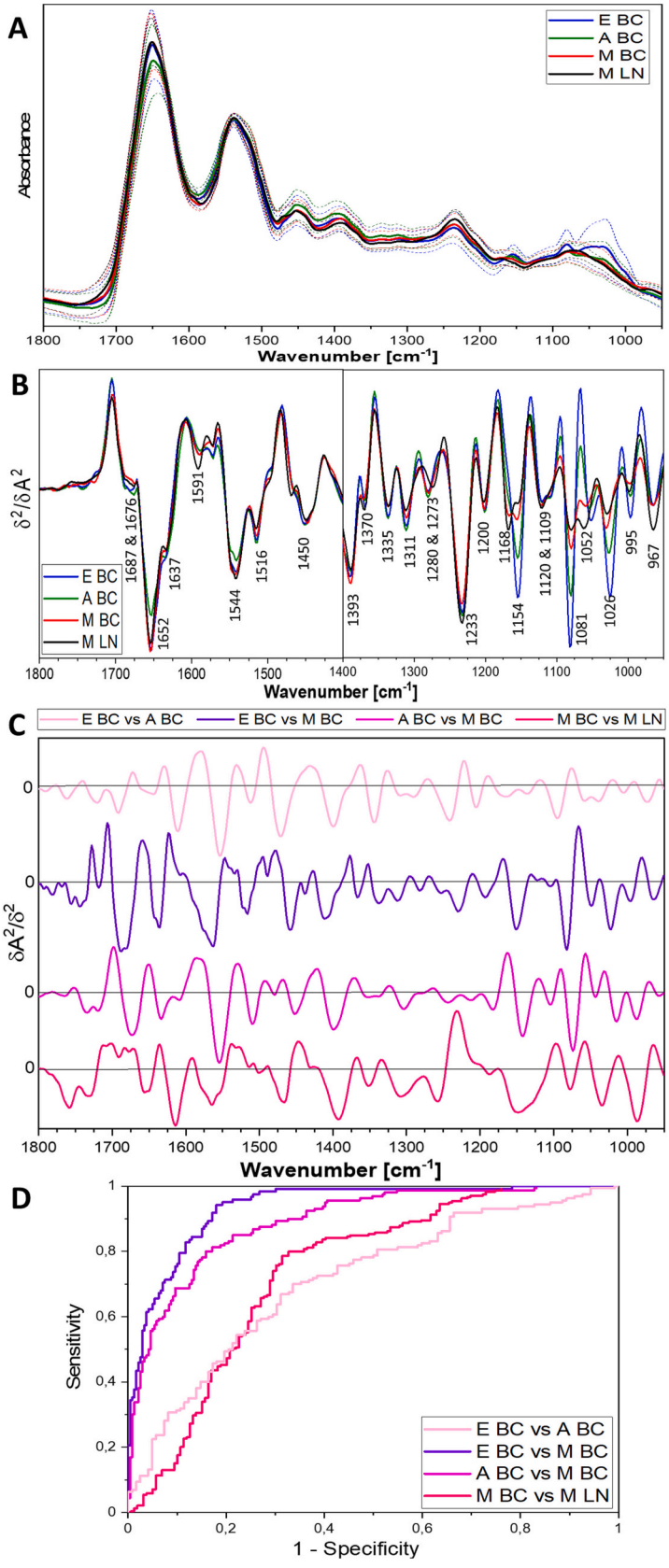

Fig. 3. A. Averaged absorbance FTIR spectra of the investigated groups of the tumors ($N_{E\ BC} = 223$, $N_{A\ BC} = 160$, $N_{M\ LN} = 170$, and $N_{M\ BC} = 241$); dashed lines - standard deviation (±SD). B. Averaged second derivative FTIR spectra from (A) in the regions of 1800–1400 (left) and 1400–950 cm^{-1} (right); the band assignments are in Table 2. C. PLS-DA regression vectors determined from the LOPO models on second derivative spectra in the region of 1800–950 cm^{-1}. D. ROC curves for the PLS-DA LOPO models.

Table 2
Positions of FTIR bands of bladder tumors with their assignment to vibrational modes and biomolecules.

Band [cm^{-1}]	Vibrational mode	Assignment
967	ν(CNC)	DNA
995	Ring stretch and deformation of uracil	RNA
1026	δ(C–OH)	Glycogen, collagen IV
1052	ν(C–O–C)	Glycoproteins, DNA
1081	ν(CC–OC) and ν(C—C) ν_s(PO2-)	Glycogen, glycoproteins Nucleic acids, phosphate- containing molecules
1119–1111	ν(C—O), ν(CC-OC)	RNA, glycoproteins
1154	ν_{as}(CO-O-C)	Glycogen, glycoproteins, hydroxyproline residue
1168	ν(COH, COC)	Glycoproteins
1200	ν(COH, COC)	Collagens
1233	Amide III	Collagens
	ν_{as}(PO2-)	Nucleic acids, phosphate-containing molecules
1280	Amide III	Collagens
1311–1335	δ(CH/CH_2)	Collagens
1370–1393	ν_s(COO^-)	Free fatty acids and amino acids
1450	δ(CH_2/CH_3)	Biomolecules
1516	$\nu(CC)_{ring}$	Tyrosine residue
1544	Amide II	Proteins
1591		Free amino acids
1637	Amide I	Proteins (β-sheets): collagens, elastin
1652	Amide I	Proteins (α-helices)
1670–1690	Amide I	Proteins (β-turns)

ν – stretching mode, as – antisymmetric, s - symmetric; δ – in-plane deformation.

a great potential of IR imaging combined with the unsupervised chemometric analysis for the detection of cancer cells, see examples in Fig. 2A and B. 3–4 UHCA classes were assigned to the tumor region since their spectra showed significant heterogeneity (Fig. 2C). This observation is congruent with a plethora of morphological and biochemical features in the tumors such as cancer cell density and diameter as well as the presence of inflammation and ischemic changes and blood supply, c. f. the cyan, blue, and purple traces in Fig. 2A and C.

The visual inspection of the extracted tumor FTIR spectra within each experimental group indicated the predominant spectral diversity in the amide I and II regions (1652 and 1544 cm^{-1}) assigned to proteins (Fig. 2C). For the non-metastatic early-stage group (E BC), the cyan and blue traces attributed to the bladder tumor indicated a high content of proteins along with the accumulation of carbohydrates (1170–950 cm^{-1}, mainly glycogen) in the peripheral cancer cells. On the other hand, IR bands of collagens (1320–1200 cm^{-1}) primarily contributed to UHCA segregation of the tissue cross-section from the non-metastatic advanced BC (A BC). As expected, they are of the highest intensity in the bladder tissue surrounding the tumor (pink trace, Fig. 2C). The blue and purple classes assigned to the tumor and localized on the border with the bladder tissue still exhibited the presence of collagens implicating the invasion of cancer cells through the extracellular matrix of the bladder. In turn, the core of the tumor (the cyan class) was almost free of collagen fibers and contained an elevated level of Tyr residues (1516 cm^{-1}). The spectral variety between classes in the metastatic advanced bladder carcinoma was mainly observed in the amide I and II regions (M BC, Fig. 2C). Interestingly, clustering of the IR image of the lymph node (M LN) distinguished the reactive center (a green class) from the secondary tumor but not the tumor from the lymph node cavity (Fig. 2A and B). The IR features of the yellow-green UHCA class were assigned to B lymphocytes according to the HE morphology and anatomy of the lymph nodes and were attributed to reactive centers and the periphery of the metastasis. The blue traces in M LN represented the metastatic mass and the paracortical and medullary area composed of lymphocytes T and macrophages.

3.2. Spectral differences between tumors

Next, all UHCA FTIR spectra extracted from the tumor region were averaged within each experimental group (Fig. 3A and B). The second derivative spectra indicated numerous differences in the fingerprint region of the IR spectrum. Detailed band assignments are collected in Table 2.

We quantified the intensities of selected bands to find potential candidates for biomarkers of BC metastasis (Fig. 4). The total content of proteins, including collagens, was high and similar for the non-metastatic primary tumors (E and A BC) and it dropped down when the BC tumor had the metastatic potential (M BC) (Fig. 5A and C). A further decrease was observed in the secondary tumors in lymph nodes. The tumor body consists of cancer cells and an extracellular matrix which is a scaffold for the shape of the tumor and induces cell polarity. The cancer cells do not maintain their functions since they constantly proliferate and digest the extracellular matrix. Thus, the two spectral biomarkers can correspond to the loss of collagen IV expressions that was already linked to ECM remodeling in invasive bladder carcinoma [24]. These bands can also serve as the markers of cellularity to matrix ratio. Interestingly, we observed the appearance of the 1052 and 1168 cm^{-1} bands assigned to glycoproteins in the spectra of the M BC and M LN groups only (Fig. 3B). This suggests the production of immature matrix and tumor-associated fibrosis called desmoplasia which is often correlated with the damage of collagen cross-linkage elevated due to the metastatic process [15,25].

The high content of tyrosine residues was found in the non-invasive BC groups and then it decreased in the malignant case (M BC) as well as the secondary tumor (M LN) (Fig. 4B). This trend was congruent with our previous in vitro studies on BC cell lines and tumor progression of breast cancer to lungs [16,26]. This spectral marker may reveal the activity of tyrosine kinases that mediates cell cycle, differentiation, motility, and survival. These enzymes are also deregulated in bladder cancer due to mutations, amplification, and chromosomal abnormalities [27].

As mentioned above, the primary tumors in the E BC group exhibited the presence of high-glycogen sites. The box plot for the intensity of the glycogen band showed the wide distribution of its min-max values and consequently a large variability of the glycogen accumulation between samples in the E BC group (Fig. 4D). This implies that hypoxic glycolysis (the Warburg effect) was not uniformly enhanced in all tumor cells in E BC and was even reduced along with the increase of the malignancy potential of the primary tumor (A and M BC, Fig. 4D) [28]. We observed similar IR features in the epithelial tissue of the bladder wall and cytological samples in studies on the discrimination of high-grade and invasive BC from low-grade and non-invasive BC [18,19].

IR bands of nucleic acids also showed pronounced alternation due to the tumor invasiveness (Fig. 4E and F) The advanced and metastatic BC exhibited DNA hypermethylation implying a decrease in RNA transcription (Fig. 4E) [29]. Furthermore, the ratio of two IR bands at 967 (DNA) and 995 cm^{-1} (RNA) can be applied for monitoring nuclear – cytoplasm ratio in the primary and secondary tumors similar to the Paris system used by histopathologists (Fig. 4F) [21]. The box plots clearly showed that this parameter gradually increased from the non-metastatic to metastatic BC by a factor over 2. The nuclear volume of cancer cells in the lymph nodes further increased. In addition, min-max values also indicated a significant variety of nuclear dimensions in M BC and M LN compared to E BC and A BC.

3.3. Classification models

Next, we employed PLS-DA to assess the classification power of IR features for the automatic recognition of metastatic bladder cancer. Preliminary classifications were created validating with LOPO cross-validation to obtain an initial estimation of the discrimination and to study the regression vectors. The statistical significance of these models

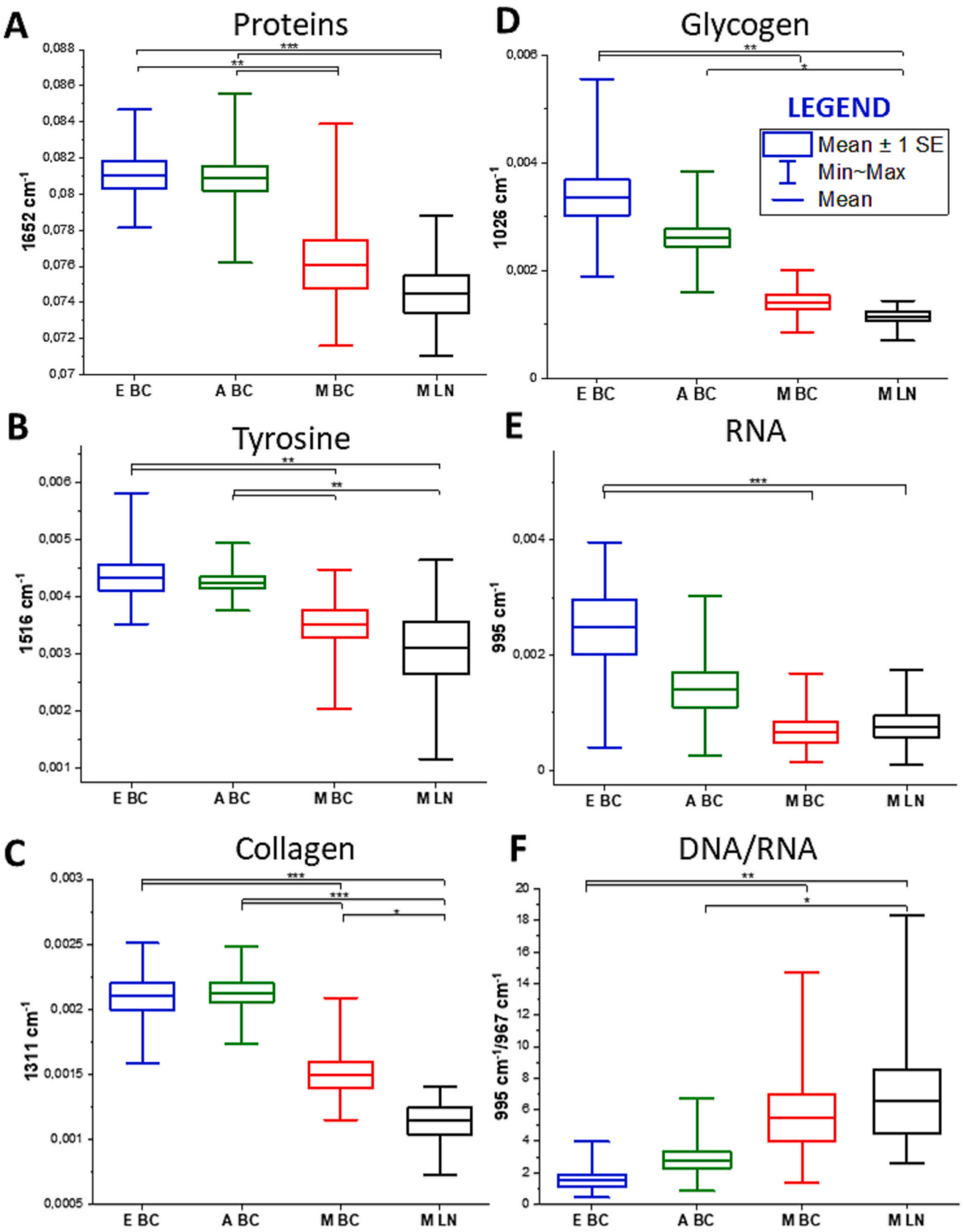

Fig. 4. Diagrams representing semi-quantitative analysis of biomolecules in the early (E BC), advanced (A BC), and metastatic BC (M BC) and secondary tumors in lymph nodes (M LN). (A) proteins (1652 cm^{-1}), (B) tyrosine (1516 cm^{-1}), (C) collagen (1311 cm^{-1}), (D) glycogen (1026 cm^{-1}), (E) RNA (995 cm^{-1}), and (F) DNA/RNA ratio (967:995 cm^{-1}). The results in the graphs are presented as dot plots with the mean, standard error (SE), and min-max values. Statistical analysis was performed by a one-way Tukey test. The symbols *, **, and *** denote statistical significance at $p < 0.05$, $p < 0.01$, and $p < 0.01$, respectively.

Table 3
Results of the Monte Carlo Double Cross Validation (MC-DCV) PLS-DA models.

Groups	AUROC	Specificity	Sensitivity	Accuracy	p-Value[a]
E BC vs A BC	0.64 ± 0.10	0.67 ± 0.11	0.52 ± 0.14	0.61 ± 0.08	<0.05
E BC vs M BC	0.93 ± 0.05	0.85 ± 0.17	0.83 ± 0.13	0.83 ± 0.08	<0.001
A BC vs M BC	0.88 ± 0.07	0.80 ± 0.13	0.75 ± 0.19	0.73 ± 0.10	<0.001
M BC vs M LN	0.66 ± 0.15	0.70 ± 0.20	0.55 ± 0.24	0.65 ± 0.12	<0.05

AUROC – area under the receiver operating characteristic.
[a] Significance value of a permutation test in a LOPO-CV using the entire dataset.

Table 4
The major regression vectors of PLS-DA LOPO models (ve-: negative and ve+: positive values; in cm^{-1}).

E BC vs A BC		E BC vs M BC		A BC vs M BC		M BC vs M LN	
ve-	ve+	ve-	ve+	ve-	ve+	ve-	ve+
1611	1580	1685	1727	1673	1697	1614	1229
1554	1493	1634	1706	1554	1651	1564	
1473		1564	1660	1518	1583	1467	
1400		1457	1623	1397	1530	1394	
		1150	1065	1143	1163	1150	
		1082		1075	1057	1034	
		1020		1022		986	

was evaluated using permutations. Finally, models with a stricter evaluation of the classification performance were obtained using repeated random sampling double cross-validation. Figures of merit can be found in Tables 3, 4 and Fig. 3C, D. To interpret these results also in terms of the spectral and molecular similarity of the primary and secondary BC tumors, we determined the model parameters for E BC, A BC, and M LN versus M BC as well as for E BC versus A BC. For the latter, all parameters were in the range of 0.52–0.67 pointing to the fact that IR spectra of cancer cells in the bladder tumors are not good indicators of the BC stage. This observation was consistent with the IR biomarkers displayed in Fig. 4 which indicated the discrimination of the early and advanced BC groups only in the spectral region below 1300 cm^{-1}. We have previously reported that BC grades and stages are well discriminated from IR spectra of the epithelial layer in the bladder. [18] Next, the IR spectra of the primary tumors were classified as E BC and M BC with a specificity of 85 % and a sensitivity of 83 % with the highest AUROC value among all groups (0.93) (Table 3 and Fig. 3D). A model for the differentiation between A BC and M BC also showed a very good prediction level with specificity, sensitivity, and AUROC of 80 %, 75 %, and 0.88, respectively. These results indicate the high capacity of FTIR spectroscopy to classify the metastatic spread of bladder cancer to lymph nodes. In the histological assessment, non-metastatic and metastatic tumors in the bladder are similar to each other and it is impossible to distinguish them by morphology the of cancer cells stained with hematoxylin and eosin.

Interestingly, the M BC vs. M LN model had a low prediction ability with an accuracy of 65 % (Table 3). We did not aim to discriminate the primary and secondary tumors for clinical purposes, but we wanted to assess whether the bladder cancer cells preserve their biochemical features after they migrate to the surrounding lymph nodes. The PLS-DA results confirmed our above observations that the spectral profile of the metastatic BC is more like the tumor in the lymph node than non-metastatic bladder tumors. All investigated BC tumors contained a tiny number of lymphocytes in different areas and the income of these lymphocytes to the spectra is low. Why then are the metastatic, secondary tumor spectra like those of lymphocytes? The M LN cancer cells might consume lymphocytes and lymph node matrix. The spectral similarity of M BC and lymphocytes could be caused by the crosstalk of lymphocytes and BC cells, probably through microvesicles and convergence of metabolism pathways and escape from some harmful factors [30]. Indeed, the tumor microenvironment (TME) in M BC and M LN is similar in terms of its overall biochemical composition. Certainly, molecular processes inducing metastasis strongly depend on a molecular signaling interplay between cancer cells, TME cells, and the immune response. The presence of lymphocytes incorporated into TME in the bladder and lymph node through microvesicles and then the convergence of metabolism pathways very likely contribute to the observed similarity of M BC and M LN [7,30].

4. Conclusions

This proof-of-concept study shows that FTIR spectroscopy imaging has significant potential to predict metastasis of bladder tumors to the regional lymph nodes with the Receiver Operating Characteristic of over 0.88. This result is excellent for a small sample cohort and considering the lack of clinical tools detecting BC metastasis. Our results showed that the spectral fingerprint of neoplastic cells is only required for modeling so there is no need to scan large tissue areas to obtain an appropriate data set. Thus, it can minimize data collection time. This fact also opens further development of FTIR-based intraoperative surgical tools to guide surgical procedures from fresh tumor samples.

Our studies indicated that there are distinct biochemical differences between the bladder tumor biopsies collected in cystoscopy and they allow for the prediction of metastasis to lymph nodes. Furthermore, the metastatic features of the primary BC tumor are still present in the secondary tumors in lymph nodes. Since these results of our work are very promising, further studies on FTIR-based features of metastasis to other distant organs would be helpful for the determination of a precise mechanism of BC metastasis. In addition, the established classification models can help make clinical decisions at the stage of cystoscopy, lymphadenectomy, and chemotherapy. Undoubtedly, this can facilitate clinical tasks aimed at reducing unnecessary procedures and accelerating the implementation of appropriate treatment.

CRediT authorship contribution statement

Conceptualization: all authors; methodology: M.K., D.P.G., K.M; histological examination: M.K., K.O.; spectral analysis and visualization: M.K., D.P.G.; draft preparation: M.K., D.P.G.; writing – review and editing: P.Ch., K.O., K.M.; supervision: K.O., K.M; project administration: M.K., K.M.

Declaration of competing interest

The authors declare that they have no known competing financial interests or personal relationships that could have appeared to influence the work reported in this paper.

Data availability

Data will be made available on request.

Acknowledgements

MK thanks the National Science Centre in Poland (Preludium 16, no. UMO-2018/31/N/NZ4/00911) and the InterDokMed project (no. POWR.03.02.00-00-I013/16) for financial support. MK thanks Joanna Wohlman from the University Children's Hospital in Krakow for cutting tissue slides. This research was also funded by the Digiworld Priority Research Area under the program Excellence Initiative – Research University at the Jagiellonian University in Krakow (granted to KM). D. P.-G. acknowledges the financial support of the 2019 Ramón y Cajal (RYC) Contract Aids (RYC2019-026556-I) funded by MCIN/AEI/10.13039/501100011033 y FSE "El FSE invierte en tu futuro" and Grant

RPID2020-119326RA-I0 funded by MCIN/AEI/10.13039/501100011033.

References

[1] H.W. Kang, W.J. Kim, W. Choi, S.J. Yun, Tumor heterogeneity in muscle-invasive bladder cancer, Transl. Androl. Urol. 9 (2020) 2866–2880, https://doi.org/10.21037/tau.2020.03.13.

[2] J.A. Witjes, H.M. Bruins, A. Carrión, R. Cathomas, E.M. Compérat, J.A. Efstathiou, R. Fietkau, G. Gakis, A.G. Van Der Heijden, A. Lorch, R.P. Meijer, M.I. Milowsky, V. Panebianco, M. Rink, G.N. Thalmann, E. Veskimäe, P.A.J. Redlef, S. Sæbjørnsen, Muscle-invasive and Metastatic Bladder Cancer EAU Guidelines on, 2022.

[3] M. Perera, S. McGrath, S. Sengupta, J. Crozier, D. Bolton, N. Lawrentschuk, Pelvic lymph node dissection during radical cystectomy for muscle-invasive bladder cancer, Nat. Rev. Urol. 15 (2018) 686–692, https://doi.org/10.1038/s41585-018-0066-1.

[4] A.S. Merseburger, A.B. Apolo, S. Chowdhury, N.M. Hahn, D. Matthew, M. I. Milowsky, D. Petrylak, T. Powles, D.I. Quinn, Therapy for Metastatic Bladder Cancer 37, 2020, pp. 95–105, https://doi.org/10.1007/s00345-018-2486-1.SIU-ICUD.

[5] E. El Rassy, Z. Bakouny, F. Aoun, F.G. Haddad, G. Sleilaty, T. Assi, J. Kattan, A network meta-analysis of the PD(L)-1 inhibitors in the salvage treatment of urothelial bladder cancer, Immunotherapy. 10 (2018) 657–663, https://doi.org/10.2217/imt-2017-0190.

[6] V.G. Martinez, E. Munera-Maravilla, A. Bernardini, C. Rubio, C. Suarez-Cabrera, C. Segovia, I. Lodewijk, M. Dueñas, M. Martínez-Fernández, J.M. Paramio, Epigenetics of bladder cancer: where biomarkers and therapeutic targets meet, Front. Genet. 10 (2019) 1–27, https://doi.org/10.3389/fgene.2019.01125.

[7] C. Luo, B. Huang, Y. Wu, Y. Xu, W. Ou, J. Chen, L. Chen, Identification of lymph node metastasis–related key genes and prognostic risk model in bladder cancer by co-expression analysis, Front. Mol. Biosci. 8 (2021) 1–9, https://doi.org/10.3389/fmolb.2021.633299.

[8] A.B. Shinagare, N.H. Ramaiya, J.P. Jagannathan, F.M. Fennessy, M.-E. Taplin, A. D. Van den Abbeele, Metastatic pattern of bladder cancer: correlation with the characteristics of the primary tumor, Am. J. Roentgenol. 196 (2011) 117–122, https://doi.org/10.2214/AJR.10.5036.

[9] S.K. Williams, F. Rabbani, Complications of lymphadenectomy in urologic surgery, Urol. Clin. North Am. 38 (2011) 507–518, vii, https://doi.org/10.1016/j.ucl.2011.07.013.

[10] M. Joseph, D. Enting, Immune responses in bladder cancer-role of immune cell populations, in: Prognostic Factors and Therapeutic Implications 9, 2019, pp. 1–15, https://doi.org/10.3389/fonc.2019.01270.

[11] R.M. da Silva, B. Pupin, T.T. Bhattacharjee, M.A. Vamondes Kulcsar, M. Uno, R. Chammas, R. de Azevedo Canevari, ATR-FTIR spectroscopy and CDKN1C gene expression in the prediction of lymph nodes metastases in papillary thyroid carcinoma, Spectrochim. Acta Part A Mol. Biomol. Spectrosc. 228 (2020) 117693, https://doi.org/10.1016/j.saa.2019.117693.

[12] B. Bird, K. Bedrossian, N. Laver, M. Miljković, M.J. Romeo, M. Diem, Detection of breast micro-metastases in axillary lymph nodes by infrared micro-spectral imaging, Analyst. 134 (2009) 1067–1076, https://doi.org/10.1039/b821166c.

[13] V. Untereiner, O. Piot, M.-D. Diebold, O. Bouché, E. Scaglia, M. Manfait, Optical diagnosis of peritoneal metastases by infrared microscopic imaging, Anal. Bioanal. Chem. 393 (2009) 1619–1627, https://doi.org/10.1007/s00216-009-2630-2.

[14] K. Augustyniak, K. Chrabaszcz, A. Jasztal, M. Smeda, G. Quintas, J. Kuligowski, K. M. Marzec, K. Malek, High and ultra-high definition of infrared spectral histopathology gives an insight into chemical environment of lung metastases in breast cancer, J. Biophotonics 12 (2019), https://doi.org/10.1002/jbio.201800345.

[15] K. Chrabaszcz, K. Kaminska, C.L. Song, J. Morikawa, M. Kujdowicz, E. Michalczyk, M. Smeda, M. Stojak, A. Jasztal, S.G. Kazarian, K. Malek, Fourier transform infrared polarization contrast imaging recognizes proteins degradation in lungs upon metastasis from breast cancer, Cancers (Basel). 13 (2021) 1–16, https://doi.org/10.3390/cancers13020162.

[16] K. Chrabaszcz, A. Jasztal, M. Smęda, B. Zieliński, A. Blat, M. Diem, S. Chlopicki, K. Malek, K.M. Marzec, Label-free FTIR spectroscopy detects and visualizes the early stage of pulmonary micrometastasis seeded from breast carcinoma, Biochim. Biophys. Acta-Mol. Basis Dis. 2018 (1864) 3574–3584, https://doi.org/10.1016/j.bbadis.2018.08.022.

[17] M. Smeda, A. Jasztal, E.H. Maleki, A. Bar, M. Sternak, G. Kwiatkowski, J. Suraj-Prażmowska, B. Proniewski, A. Kieronska-Rudek, K. Wojnar-Lason, K. Skrzypek, M. Majka, K. Chrabaszcz, K. Malek, S. Chlopicki, Endothelial-mesenchymal transition induced by metastatic 4T1 breast cancer cells in pulmonary endothelium in aged mice, Front. Mol. Biosci. 9 (2022) 1–17, https://doi.org/10.3389/fmolb.2022.1050112.

[18] M. Kujdowicz, D. Perez-Guaita, P. Chlosta, K. Okon, K. Malek, Evaluation of grade and invasiveness of bladder urothelial carcinoma using infrared imaging and machine learning, Analyst. 148 (2023) 278–285, https://doi.org/10.1039/d2an01583h.

[19] M. Kujdowicz, B. Mech, K. Chrabaszcz, P. Chlosta, K. Okon, K. Malek, FTIR spectroscopic imaging supports urine cytology for classification of low- and high-grade bladder carcinoma, Cancers (Basel). 13225734 (2021).

[20] M. Kujdowicz, D. Perez Guaita, P. Chłosta, K. Okon, K. Malek, Towards the point of care and noninvasive classification of bladder cancer from urine sediment infrared spectroscopy. Spectral differentiation of normal, abnormal and cancer patients, Microchem. J. 168 (2021), 106460, https://doi.org/10.1016/j.microc.2021.106460.

[21] V.E.R. Holger Moch, Peter A. Humphrey, Thomas M. Ulbright, WHO Classification of Tumours of the Urinary System and Male Genital Organs, 4th ed., 2016.

[22] P. Lasch, CytospecTM. A Matlab Based Application for Infrared Imaging, 2001.

[23] D. Pérez-Guaita, J. Kuligowski, S. Garrigues, G. Quintás, B.R. Wood, Assessment of the statistical significance of classifications in infrared spectroscopy based diagnostic models, Analyst. 140 (2015) 2422–2427, https://doi.org/10.1039/c4an01783h.

[24] A. Brunner, A. Tzankov, The role of structural extracellular matrix proteins in urothelial bladder cancer (review), Biomark. Insights 2 (2007) BMI.S294, https://doi.org/10.4137/BMI.S294.

[25] A.M. Fuller, T.S.K. Eisinger-Mathason, Context matters: response heterogeneity to collagen-targeting approaches in desmoplastic cancers, Cancers (Basel). 14 (2022), https://doi.org/10.3390/cancers14133132.

[26] M. Kujdowicz, W. Placha, B. Mech, K. Chrabaszcz, K. Okoń, K. Malek, In vitro spectroscopy-based profiling of urothelial carcinoma: a Fourier transform infrared and Raman imaging study, Cancers (Basel). 13 (2021) 123, https://doi.org/10.3390/cancers13010123.

[27] A.S. Zangouei, A.H. Barjasteh, H.R. Rahimi, M. Mojarrad, M. Moghbeli, Role of tyrosine kinases in bladder cancer progression: an overview, Cell Commun. Signal. 18 (2020) 1–14, https://doi.org/10.1186/s12964-c020-00625-7.

[28] J. Lu, M. Tan, Q. Cai, The Warburg effect in tumor progression: mitochondrial oxidative metabolism as an anti-metastasis mechanism, Cancer Lett. 356 (2015) 156–164, https://doi.org/10.1016/j.canlet.2014.04.001.

[29] S. Harsanyi, Z.V. Novakova, K. Bevizova, L. Danisovic, S. Ziaran, Biomarkers of bladder cancer: cell-free DNA, epigenetic modifications and non-coding RNAs, Int. J. Mol. Sci. 23 (2022), https://doi.org/10.3390/ijms232113206.

[30] R. Sullivan, G. Maresh, X. Zhang, C. Salomon, J. Hooper, D. Margolin, L. Li, The Emerging Roles of Extracellular Vesicles As Communication Vehicles Within the Tumor Microenvironment and Beyond 8, 2020, pp. 1–11, https://doi.org/10.3389/fendo.2017.00194.